

Article

Geochemical Insights from Clinopyroxene Phenocrysts into the Magma Evolution of an Alkaline Magmatic System from the Sanshui Basin, South China

Peijia Chen ¹, Nianqiao Fang ^{1,*} and Xiaobo Yuan ^{1,2}

¹ School of Ocean Science, China University of Geoscience (Beijing), Beijing 100083, China; 3011180003@cugb.edu.cn (P.C.); yuanxiaobo2011@163.com (X.Y.)

² Marine Science Research Center, Hebei Normal University of Science & Technology, Qinhuangdao 066004, China

* Correspondence: fangnq@cugb.edu.cn

Abstract: The Sanshui Basin is located at the northern continental margin of the South China Sea and characterized by a continental rift basin. The bimodal volcanic rocks in Sanshui Basin record the early Cenozoic magmatic activity in the South China Block, but the magmatic evolution that produced the bimodal volcanic rocks is poorly understood. Clinopyroxenes in bimodal volcanic rocks in the Sanshui Basin provide an opportunity to investigate magma during magma ascent. In this work, we classified nine types of clinopyroxene phenocrysts according to composition and texture in cogenetic basalt-trachyandesite-comenditic trachyte, while the composition of unzoned clinopyroxene have an evolution sequence of diopside-hedenbergite-aegirine along with an increase in trace element contents with a decrease of Mg[#], indicating that the genesis of clinopyroxene was dominated by fractional crystallization in a closed magma system. However, the clinopyroxenes with reversed zoning and multiple zoning record the process of magma mixing and recharge indicating an open magma system. While fractional crystallization is the dominant process, magma mixing, recharge, and crystal settling were also found to influence magma evolution. Thermobarometric calculations showed that clinopyroxene crystallized a several structural levels in the crust during magma ascent. In this study, we established a magma plumbing system that provides new constraints for the magma evolution in the Sanshui Basin.

Keywords: Sanshui Basin; clinopyroxene phenocryst; thermobarometry; magma mixing; fractional crystallization



Citation: Chen, P.; Fang, N.; Yuan, X. Geochemical Insights from Clinopyroxene Phenocrysts into the Magma Evolution of an Alkaline Magmatic System from the Sanshui Basin, South China. *Minerals* **2021**, *11*, 1295. <https://doi.org/10.3390/min11111295>

Academic Editors: Sergei Khromykh and Andrei Tsygankov

Received: 27 October 2021

Accepted: 19 November 2021

Published: 22 November 2021

Publisher's Note: MDPI stays neutral with regard to jurisdictional claims in published maps and institutional affiliations.



Copyright: © 2021 by the authors. Licensee MDPI, Basel, Switzerland. This article is an open access article distributed under the terms and conditions of the Creative Commons Attribution (CC BY) license (<https://creativecommons.org/licenses/by/4.0/>).

1. Introduction

The study of volcanic rocks could help us investigate deep magma chamber processes and their evolutionary history. Magma chamber processes such as magma mixing, recharge, crystal mush remobilization, fractional crystallization, and assimilation are all part of the magma evolution process and can trigger volcanic eruptions [1–3]. However, these processes may not always be documented in the whole-rock composition of volcanic rocks if the mixing process is efficient [2,4–6]. When magma ascends from deep to shallow, changes in physical and chemical conditions affect the texture and composition of minerals; these changes may be recorded and preserved in the affected minerals [7,8].

Clinopyroxene is an important rock-forming mineral in volcanic rocks due to its wide crystallization range. The textural characteristics and compositional zoning of clinopyroxene record magmatic crystallization history and constrain magma storage conditions, which provides an opportunity to investigate the processes during magma ascent [2,9,10]. Clinopyroxene has been studied worldwide for a long period of time [2,7,11–20]. Granular scale studies of clinopyroxene with different textures and compositions can be used to distinguish open- and closed-magma systems and provide the evidence necessary to unravel the evolution of magma systems and establish magma plumbing systems [1,2,11].

The Sanshui Basin is a continental rift basin distributed along the NE trend in the northern continental margin of the South China Sea. The bimodal volcanic rocks in this basin consist of alkaline basalt and peralkaline felsic rocks that record the early Cenozoic magmatism in the South China Block and represent the beginning of the large-scale extensional event and mantle upwelling in the region [21]. The widely distributed bimodal volcanic rocks of the Sanshui Basin are also noteworthy because the basalt is mantle-derived, with peralkaline felsic volcanic rocks subsequently generated by fractional crystallization in the crust [22,23]. However, the processes that produce the bimodality are not yet clear. Zhang [24] studied rare tholeiitic magma mixing in clinopyroxene from alkaline basalt of the Sanshui Basin, but the more abundant clinopyroxene in basaltic and felsic end-member rocks has been much less commonly studied. In this paper, we report the major and trace element characteristics of clinopyroxene with different textural characteristics in the cogenetic basalt-trachyandesite-comenditic trachyte magma of the Sanshui Basin. By integrating the modelling of whole-rock geochemical signatures attributed to fractional crystallization, we establish an appropriate magma plumbing system through thermo-barometric estimates of P-T conditions of clinopyroxene growth, with the ultimate goal to establish the structure of the magma plumbing in the Sanshui Basin and reveal the tectonic evolution of the northern continental margin of the South China Sea during the early Cenozoic.

2. Geologic Setting

The Sanshui Basin is located in the northern continental margin of the South China Sea, and is a sedimentary-volcanic basin with continental rift characteristics developed in the Late Cretaceous to Late Eocene [25]. Constrained by the NE-trending Sihui-Wuchuan Fault, NW-trending Gangyao-Shawan Fault, and Xijiang Fault, the Sanshui Basin has a rhomboid geometry with a north-south-trending eruption axis, covering an area of about 3300 km² [25,26]. The crustal thickness of the Sanshui Basin (27–28 km) is significantly thinner than that of Wuyi-Nanling fold zone in the north (30–33 km) and presents a high Bouguer gravity anomaly, due to crustal extension [25,27].

During the contemporaneous stratigraphic deposition in the Sanshui Basin, there was extensive bimodal volcanic activity between 60 Ma and 38 Ma [28]. Although basalts are rare in surface outcrops, drilling has revealed that there are more than 1000 m of volcanic rocks beneath the Sanshui Basin [26]. Basalts are found in Zidong, Jiangbian, Wangjiegang, JiliXu, and Shitoucun in the center of the basin (Figure 1). The rocks mainly including olivine basalt and olivine tholeiite with OIB characteristics [28,29]. Compared to the geographically scattered distribution of basalt, felsic volcanic rocks are concentrated in the Shiling-Zoumaying in the north and Xiqiao Mountain in the south. The peak period of felsic volcanism was 55–56 Ma. The geochemical characteristics of silicic volcanic rocks are weakly peralkaline, comenditic trachyte, comendite, and pantellerite. These peralkaline felsic volcanic rocks have the characteristics of A1-type rhyolite [28]. Trachyandesite is exposed near the southern Xiqiao Mountain, and its geographic range is limited.

The basalt and peralkaline felsic volcanic rocks in the Sanshui Basin have similar trace elements and REE distribution patterns and features similar $\epsilon\text{Nd}(t)$ isotopic compositions. Thus, these rocks are considered to be the results of cogenetic magmatic evolution, through which mantle-derived basalts generated peralkaline felsic volcanic rocks via long-term fractional crystallization in the shallow crust [22,23].

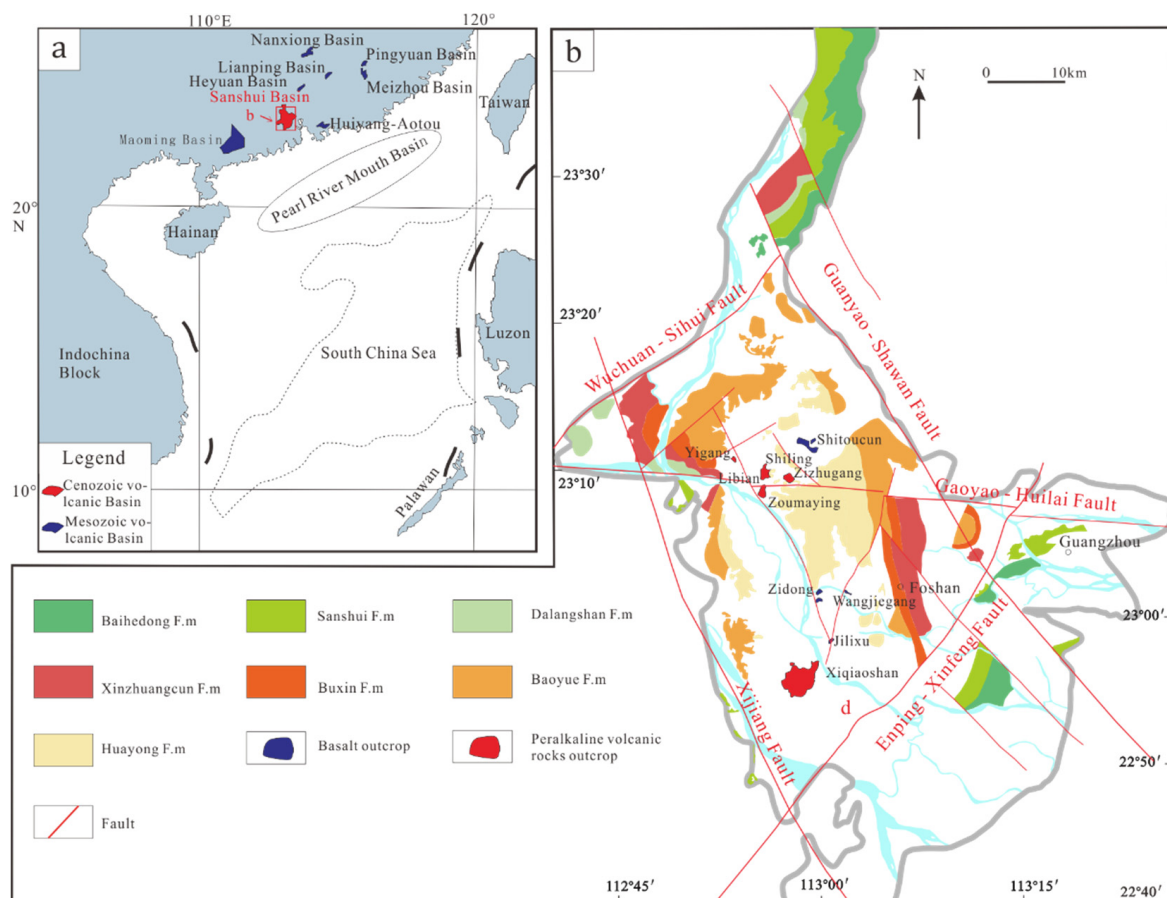


Figure 1. (a) Distribution map of volcanic basins to the northern continental margin of the South China Sea. (b) Geological map of the Sanshui Basin.

3. Materials and Methods

Sample were taken from the Sanshui Basin. After examining the textures and petrography of the volcanic rocks under a microscope at the School of Ocean Science of China University of Geosciences Beijing (CUGB), we used polished sections of these volcanic rocks to conduct Electron-Probe Micro-Analysis (EPMA) and in situ trace element analyses of the clinopyroxene phenocrysts.

The major elements were analyzed with an EMPA-1600 Superprobe at the State Key Laboratory of Geological Process and Mineral Resources of CUGB. Operating conditions of a 15 kV accelerating voltage, 10 nA beam current, and 5 mm beam diameter were used for clinopyroxene analysis. Natural minerals and synthetic oxides (SPI Company of America), including olivine (for Si and Mg), rutile (for Ti), albite (for Al, Na, and K), garnet (for Fe), rhodonite (for Mn), diopside (for Ca), and chromite (for Cr), were used for electron micro-probe calibration. The precision was better than 1 wt. % for the element oxides.

Trace element compositions of clinopyroxene were determined on a Bruker M90 ICP-MS equipped with a RESOLUTION S-155 195 nm excimer laser-ablation system at the Institute of Mineral Resources, Chinese Academy of Geological Sciences, Beijing (CAGS). Helium was applied as a carrier gas, which was mixed with argon to lower the detection limit and improve the precision. Each analysis consisted of a background acquisition of approximately 15 s (gas blank) followed by 45 s of data acquisition from the sample. Detailed information regarding the operation steps of the LA-ICP-MS was provided by Liu [30]. Element contents were calibrated against multiple reference materials (BCR-2G, NIST 610, and GSE-1G), and the Ca abundance measured by EPMA was as an internal standard [31]. The preferred values of element concentrations for these USGS glasses were obtained from the GeoReM database (<http://georem.mpch-mainz.gwdg.de/>, accessed on 20 November

2021). The off-line selection and integration of background and analyte signals, time-drift correction, and quantitative calibration were performed using ICPMSDataCal 10.8 [30,31]. The analysis of most of the elements presented an accuracy of less than 5% and a precision greater than 10%.

4. Petrography and Mineralogy

4.1. Characteristics of Petrography

Basalts in the Sanshui Basin exhibit a porphyritic seriate texture (porphyritic index, P.I. = 25–35%, Figure 2a,b) with olivine (~5%), clinopyroxene (~7%), and plagioclase (~18%) phenocrysts, set in a microcrystalline groundmass of the same phases plus Ti-Fe oxide and apatite as accessory minerals. Olivine (Fo61 to Fo83) phenocrysts are usually serpentinized at the rims and cracks, clinopyroxene phenocrysts are usually euhedral and fresh, and plagioclase (An44–An76) is euhedral-subhedral tabular.

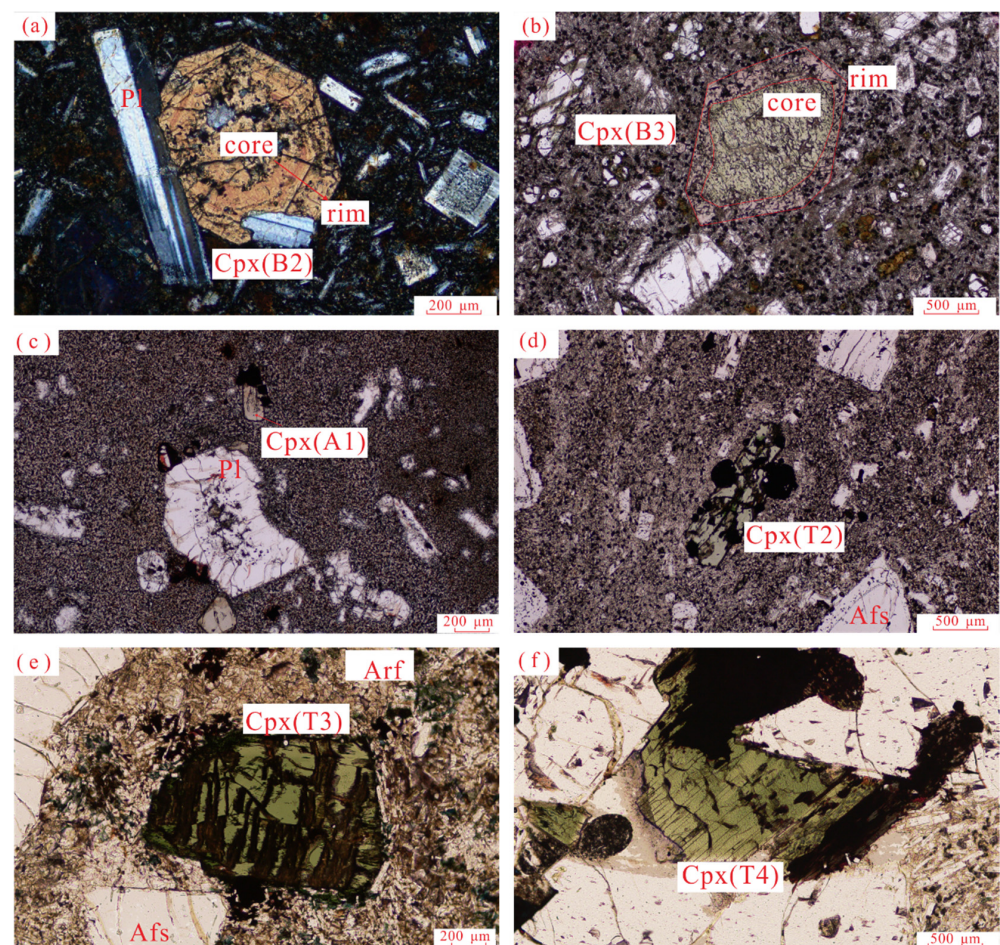


Figure 2. Characteristics of representative clinopyroxene in bimodal volcanic rocks in the Sanshui Basin. (a) B2 type clinopyroxene phenocryst and plagioclase phenocryst in basalt, where the zoning texture can be observed in clinopyroxene, 18ss082-1; (b) B3 type clinopyroxene phenocryst in basalt, with a green core and a light yellow rim, 17ss063-1; (c) A1 type clinopyroxene phenocryst in trachyandesite, 18ss014-1; (d) T2 type clinopyroxene phenocryst and coexisting titan-magnetite in comenditic trachyte, 19ss027-1; (e) T3 type clinopyroxene phenocryst in comenditic trachyte, and amounts of arfvedsonite distributed in the groundmass, 17ss054-1; (f) T4 type clinopyroxene coexisting with alkali feldspar in comenditic trachyte, 14ss003-5. Cpx = clinopyroxene, Pl = plagioclase, Afs = alkali feldspar, Arf = arfvedsonite.

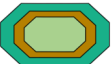
Trachyandesite exhibit a porphyritic seriate texture (P.I. = 10–12%, Figure 2c) with olivine (~1%), clinopyroxene (~3%), and plagioclase (~7%) phenocrysts and lesser amounts of K-feldspar, set in a microcrystalline groundmass of the same phases plus Ti-Fe oxide and apatite as accessory minerals.

The clinopyroxene phenocrysts in peralkaline felsic volcanic rocks occur only in comenditic trachyte. Comenditic trachyte exhibit a porphyritic seriate texture (P.I. = 8–15%, Figure 2d,e), mainly with mainly alkaline feldspar (~6–13%) phenocrysts and lesser amounts of clinopyroxene (~0–2%), arfvedsonite, and Ti-Fe oxide phenocrysts, set in a microcrystalline groundmass of the same phases with accessory minerals including haleniusite, apatite, monazite, pyrochlore, and zircon. Clinopyroxene is usually euhedral as phenocrysts or trapped in alkaline feldspar phenocrysts. There are fewer phenocrysts (P.I. = 2–5%) in pantellerite, and most are alkaline feldspar.

4.2. Characteristics of Clinopyroxene

Clinopyroxene phenocrysts are commonly observed in basalt, trachyandesite, and comenditic trachyte, but have not been found in comendite or pantellerite with greater evolution. Clinopyroxene phenocrysts are euhedral-subhedral columnar, with sizes between 0.25 mm and 4 mm. Clinopyroxene can be classified into 9 types according to their composition and textural characteristics in the bimodal volcanic rocks from the Sanshui Basin, including three types in basalts (B1, B2, and B3 type), one type in trachyandesite (A1 type), and four types in comenditic trachyte (T1, T2, T3, and T4 type). As per the previous study by Zhang [24], we added an additional B4 type in basalt. Specific classification and characteristics of clinopyroxenes are shown in Table 1, Figure 2, and Figure 3.

Table 1. Summary of the clinopyroxene textures, zoning, and chemical characteristics in the bimodal volcanic rocks.

Type	Zoning	Texture	Abundance	Description
B1	Unzoned		93	Light yellow, colorless; no discernible zoning or Mg# variations < 2
B2	Normal		5	Light yellow, colorless; gradational normal zoning with a decrease in Mg# from core to rim
B3	Reverse		1	Light green core with yellow rim, concentric zoning or patchy zoning; Mg# variations are usually >15
B4	Multiple		1	Light yellow; coarse banding zoning (100 mm); Mg# variations are usually ~ 10; reference from Zhang [24]
A1	Unzoned		100	Light yellow; Mg# = 64
T1	Unzoned		1	Light yellow; Mg# = 75
T2	Unzoned		65	Light green; Mg# variations are scattered
T3	Unzoned		33	Green; Mg# < 10
T4	Unzoned		1	Dark green; Mg# < 1

Mg# = $100 \times \text{Mg}/(\text{Mg} + \text{Fe})$, where Fe is the total iron content.

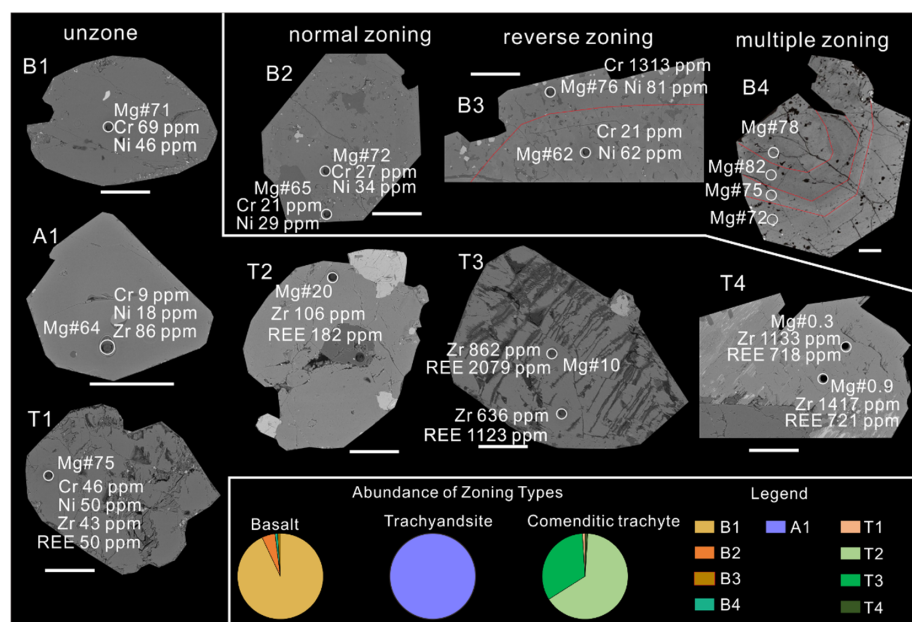


Figure 3. BSE images of selected clinopyroxene phenocrysts, highlighting different geochemical characteristics and zoning types. Pie charts show the relative proportion of each clinopyroxene type within different lithologies. Scale bars are 200 μm .

5. Results

The major and trace elements of clinopyroxene in bimodal volcanic rocks in the Sanshui Basin are listed in Tables S1 and S2. On the Wo-En-Fs diagram (Figure 4a), clinopyroxenes in basalt and trachyandesite are augite-diopsidite; T1 type clinopyroxenes are diopsidite, which have similar compositions to that clinopyroxenes in basalt; T2 type clinopyroxenes are diopsidite (Di) to hedenbergite (Hd); T3 type clinopyroxenes are hedenbergite; and T4 type clinopyroxenes are aegirine (Aeg). The same evolutionary trend can also be observed in the Aeg-Di-Hd diagram (Figure 4b), clinopyroxene compositions trend from diopsidite in basalt to hedenbergite in comenditic trachyte, and eventually to aegirine. This evolutionary trend can also be observed in other alkaline volcanic rock series [1,32]. In the Hark-type diagrams (Figure 5), it can be seen that the contents of TiO_2 , Al_2O_3 , and Cr_2O_3 are positively correlated with $\text{Mg}^\#$, while the contents of Na_2O , Mn_2O , Eu/Eu^* , and ΣREE are negatively correlated with $\text{Mg}^\#$.

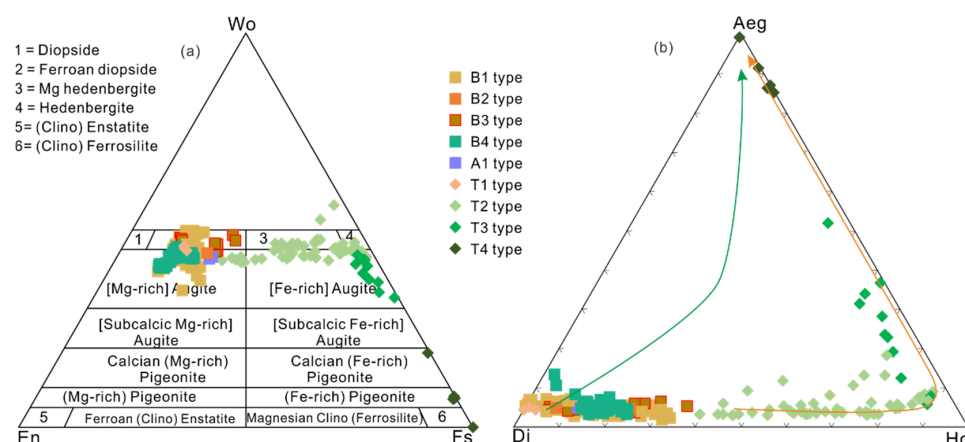


Figure 4. Clinopyroxene compositions plotted into the ternary (a) Wo-En-Fs system and (b) Aeg-Di-Hd system [33]. Some clinopyroxenes in the Sanshui Basin are from [24,28]. Clinopyroxene trends from other alkaline complexes are shown for comparison; green line [1] and orange line [32]. Wo: Ca end-member, En: Mg end-member, Fs: Fe end-member.

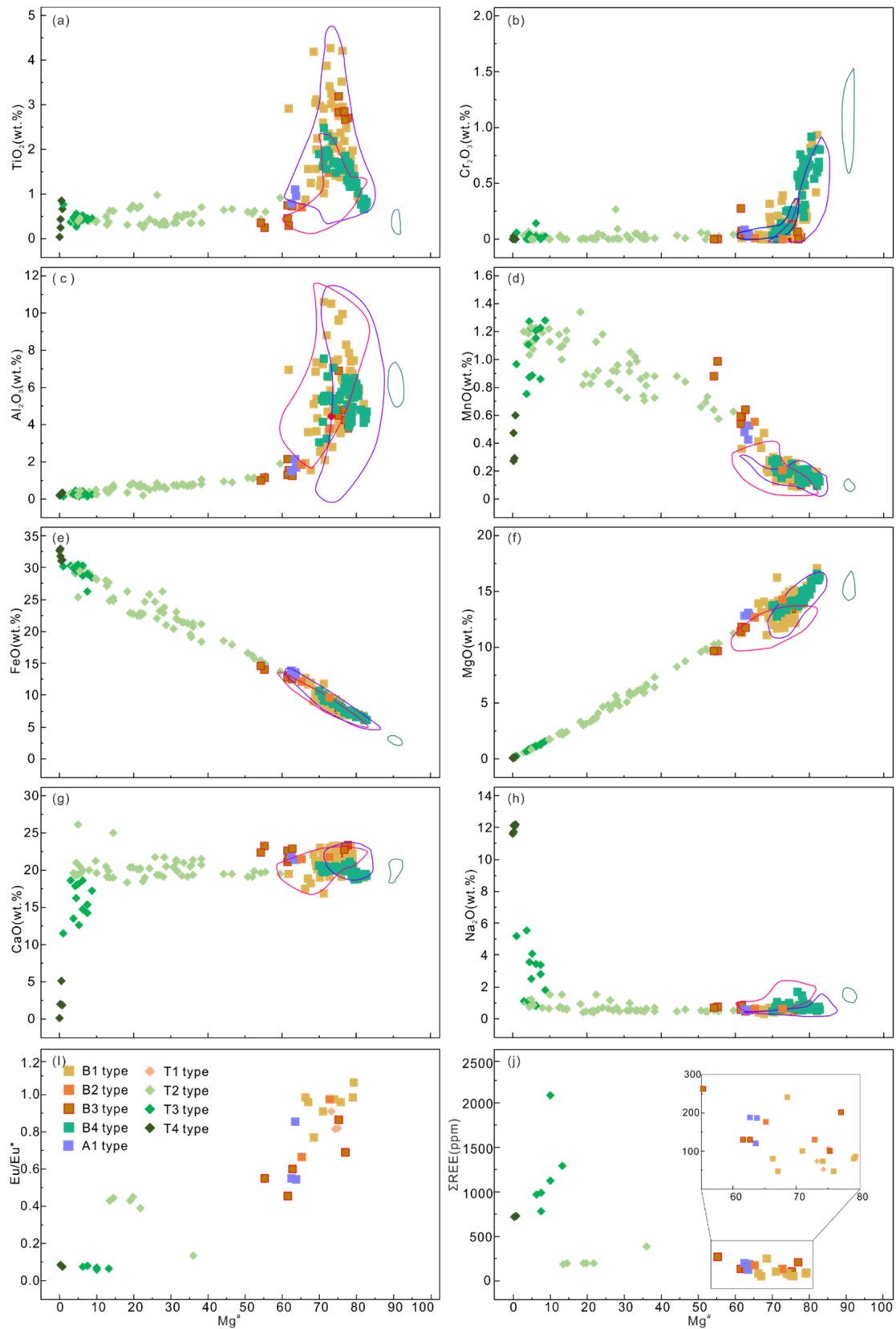


Figure 5. Major elements and REEs vs. $\text{Mg}^\#$ values in clinopyroxene from bimodal volcanic rocks in the Sanshui Basin. The green line indicates the composition of clinopyroxenes in Hannuoba granulite (North China Craton) [34]; The pink solid is the composition of clinopyroxenes in peridotite xenoliths in South China [34–36]; the purple line represents clinopyroxenes in Hainan Cenozoic basalt are from [37]. $\text{Eu}/\text{Eu}^* = \text{Eu}_N / [\text{Sm}_N + \text{Gd}_N]^{0.5}$, normalized values are from [38].

5.1. Clinopyroxene in Basalt

Whilst the compositions of B1 type clinopyroxenes in separate basalts are relatively homogeneous in perspective samples, the composition of clinopyroxenes varies widely in different basalt samples. The clinopyroxenes in Wangjiegang are characterized by $Mg^{\#}$ (72–82) and $Wo_{39.7-49.7}En_{36.6-49.3}Fs_{10.6-14.9}$; the clinopyroxenes in Jiangbian are characterized by $Mg^{\#}$ (62–76) and $Wo_{49.1-50.1}En_{36.5-40.9}Fs_{11.7-14.4}$; the clinopyroxenes in Zidong are characterized by $Mg^{\#}$ (69–73) and $Wo_{34.7-49.6}En_{34.6-46.8}Fs_{13.7-18.5}$, while the basalt is characterized by lower a $Mg^{\#}$ value (62) and $Wo_{43.3}En_{35.2}Fs_{21.5}$; the clinopyroxenes in Shitoucun are characterized by $Mg^{\#}$ (69–76) and $Wo_{32.3-45.8}En_{39.5-43.1}Fs_{13.5-16.7}$; and the clinopyroxenes in jilixu are characterized by $Mg^{\#}$ (66–73) and $Wo_{34.7-42.4}En_{39.8-41.8}Fs_{15.7-21.1}$.

The trace-elements contents of clinopyroxenes in basalt varies significantly, and the normalized REE content indicates that clinopyroxenes are enriched 8–100 times relative to the chondrite. The $Mg^{\#}$ value of B1 type clinopyroxene has no obvious relationship with trace elements, the Cr content of clinopyroxene in the 17ss066-1 sample can reach up to 2085 ppm, and the REEs contents are relatively homogeneous ($\Sigma REE = 43-99$ ppm). Moreover, the REE contents exhibit no obvious Eu anomalies ($Eu/Eu^* = 0.90-1.18$, Figure 6a) along with MREE enrichment relative to LREE and HREE ($La_N/Nd_N = 0.34-0.82$, $Tb_N/Lu_N = 1.82-3.00$, and $La_N/Yb_N = 0.71-2.53$) in Chondrite-normalized REE distribution patterns (Figure 6), reflecting different degrees of extraction from the mantle [34]. The clinopyroxene which has lower $Mg^{\#} = 62$, is characterized by a lower Eu/Eu^* of 0.76 and a higher ΣREE content of 240 ppm.

B2 type clinopyroxenes are less abundant and are characterized by normal zoning. These clinopyroxenes can be observed in clinopyroxene in 18ss082-1 from Zidong. Here, the $Mg^{\#}$ value decreases from core (73) to rim (65), and $Wo_{44.5}En_{40.6}Fs_{14.9}-Wo_{44.4}En_{36.3}Fs_{19.3}$. Compared with B1 type clinopyroxene, the core of B2 type clinopyroxene exhibits similar characteristics ($Eu/Eu^* = 0.97$, $\Sigma REE = 129$ ppm), with the rim of B2 type clinopyroxene exhibiting strongly negative Eu anomalies ($Eu/Eu^* = 0.66$) and higher REE content ($\Sigma REE = 176$ ppm).

B3 type clinopyroxenes are less abundant in the Wangjiegang sample and are characterized by reversed zoning. The green cores of B3 type clinopyroxenes have lower $Mg^{\#}$ values (55–62) and $Wo_{44.7-48.6}En_{28.2-34.4}Fs_{19.7-23.8}$, while the rims of B3 type clinopyroxenes have higher Mg values (76–78) and $Wo_{47.4-49.0}En_{38.5-40.5}Fs_{11.3-12.4}$, which are similar to the B1 type clinopyroxenes of the same sample. Similar geochemical characteristics also can be observed in trace elements. The green core of B3 type clinopyroxenes exhibited strongly negative Eu anomalies ($Eu/Eu^* = 0.54$, Figure 6c) and higher REE content ($\Sigma REE = 263$ ppm) than those in the rims ($Eu/Eu^* = 0.68$, and $\Sigma REE = 201$ ppm).

As in a previous study on B4 type clinopyroxene [24], Zhang [24] divided the area from the core to the rim into four zones. In core, the $Mg^{\#}$ value ranges from 78 to 79; in zone 1, the $Mg^{\#}$ value ranges from 80 to 83; in zone 2, $Mg^{\#}$ value ranges from 72 to 81; in rim, the $Mg^{\#}$ value ranges from 70 to 76. Core and Zone 1 exhibited the characteristics of reversed zoning, and Zone 2, and rim exhibited the characteristics of normal zoning.

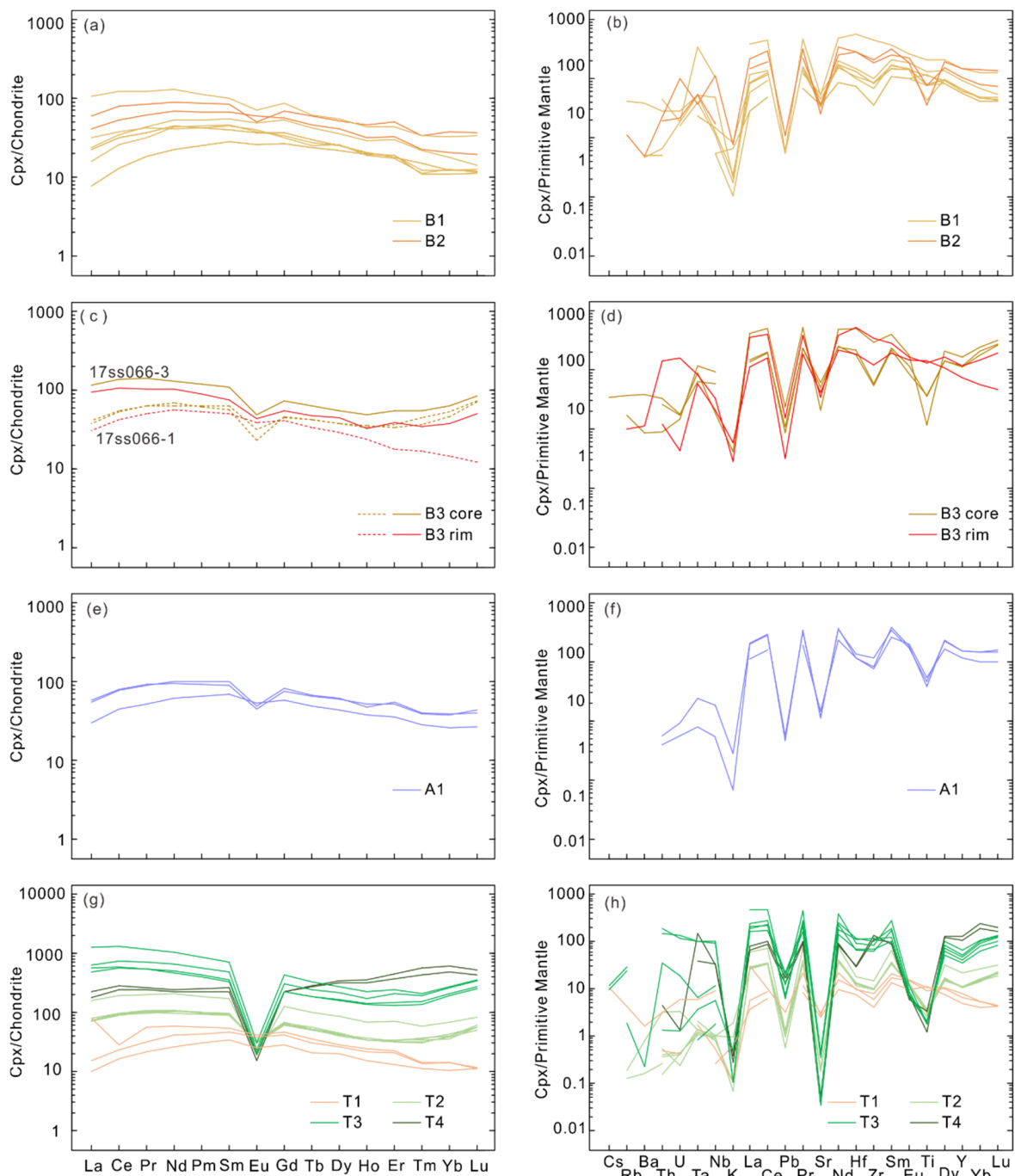


Figure 6. Chondrite-normalized REE distribution patterns and primitive mantle-normalized trace element distribution patterns for clinopyroxene from bimodal volcanic rocks in the Sanshui Basin. Normalized values are from [38].

5.2. Clinopyroxene in Trachyandesite

The compositions of A1 type clinopyroxene in trachyandesite are homogeneous and characterized by $Mg^{\#}$ (63–64) and $Wo_{34.7-49.6}En_{34.6-46.8}Fs_{13.7-18.5}$, $\Sigma REE = 120-188$ ppm, and a flat REEs distribution pattern ($La_N/Yb_N = 1.18-1.54$). There are obvious depletions in Pb, Sr, P, and K, with strongly negative Eu anomalies ($Eu/Eu^* = 0.54-0.88$, Figure 6e) in all A1 type clinopyroxene phenocrysts.

5.3. Clinopyroxene in Comenditic Trachyte

The compositions of clinopyroxenes in comenditic trachyte are relatively homogeneous, with no obvious zoning textures. Light-yellow T1 type clinopyroxenes have a

compositional range of $Wo_{45.0-46.2}En_{40.6-40.8}Fs_{13.1-14.4}$, with low Na contents (<0.05 apfu, apfu: atoms per formula unit); light-green T2 Type clinopyroxenes have a compositional range of $Wo_{42.1-56.7}En_{2.6-34.3}Fs_{27.8-54.6}$, with low Na contents (<0.15 apfu); green T3 type clinopyroxenes have a compositional range of $Wo_{33.1-42.9}En_{0.8-4.7}Fs_{54.1-66.2}$, with medium Na contents (0.20–0.45 apfu), and dark-green T4 type clinopyroxenes are similar to aegirine with a compositional range of $Q_{13.3-22.8}Jd_{0.5-1.4}Aeg_{76.4-86.0}$, and Na apfu ≈ 1 .

Similar to the major elements, the differences in trace elements in comenditic trachyte are also obvious. The content of incompatible elements in T1 to T3 type clinopyroxene are negatively correlated with $Mg^\#$. The trace-element composition of T1 type clinopyroxenes is similar to that of B1 type clinopyroxenes in basalt, which exhibits no significant Eu anomalies ($Eu/Eu^* = 0.81-0.90$, Figure 6g) and relatively low REE contents ($\Sigma REE = 50-106$ ppm). The T2 type clinopyroxenes in 20ss17-3 are characterized by significant Eu anomalies ($Eu/Eu^* = 0.39-0.44$, Figure 6a), high REE contents ($\Sigma REE = 183-197$ ppm) and LREE enrichment relative to HREE ($La_N/Yb_N = 1.82-2.35$). Another T2 type clinopyroxene in 17ss054-1 exhibited similar REE patterns to that of 20ss017-3, but showed greater evolution, with smaller Eu anomalies ($Eu/Eu^* = 0.13$) and higher REE content ($\Sigma REE = 397$ ppm). For T3 type clinopyroxenes, the grains in different samples presented similar REE patterns and significant Eu anomalies ($Eu/Eu^* = 0.06-0.08$, Figure 6a), and have various REE contents. The REE contents of T3 type clinopyroxenes in 17ss054-1 (ranging from 780 to 979 ppm) were found to be much lower in 16ss009-1 (ranging from 1123 to 2079 ppm). The composition of aegirine in T4 type clinopyroxenes shows similar Eu anomalies ($Eu/Eu^* = 0.07-0.08$, Figure 6a) and lower REE contents ($\Sigma REE = 718-722$ ppm) relative to T3 type clinopyroxenes. These clinopyroxenes are characterized by HREE enrichment relative to LREE ($La_N/Yb_N = 0.29-0.46$), which is similar to aegirine in other alkaline volcanic series [1,32].

6. Discussion

6.1. Clinopyroxene-Melt Equilibrium

The evolution of magma systems involves complex processes such as magma mixing, recharge, mush remobilization, fractional crystallization, and assimilation, which may be recorded in the compositional and textural features of clinopyroxene [1]. Three types of crystal populations are commonly classified in magmatic systems: autocrysts, antecrysts, and xenocrysts [8,11,15]. Autocrysts crystallize from the last stage of the melt and are usually in equilibrium with their host melts; antecrysts are phases that did not crystallize from the host magma, but rather from an earlier stage of the same magma system [1,18,39]; and xenocrysts are entrapped in wall-rocks or mantle xenoliths [8]. Since autocrysts are the only crystals in equilibrium with their host melts, they can be distinguished from antecrysts and xenocrysts by equilibrium testing, which is a prerequisite for the application of clinopyroxene-melt thermobarometer calculation.

Here, we consider the whole-rock composition to represent the melt composition as the bimodal volcanic rocks in the Sanshui Basin are all holocrystalline and lack other glass and melt inclusion components. The cpx-melt equilibrium conditions are calculated using the Kd_{Fe-Mg} model [40]: ${}^{cpx-liquid}Kd_{Fe-Mg} = 0.28 \pm 0.08$. The equilibrium diagram (Figure 7) shows that not all clinopyroxenes are in equilibrium with the whole-rock compositions.

The average Kd^{Fe-Mg} value of clinopyroxenes in basalt is 0.36. About 50% of clinopyroxenes, mainly B1, B2, and B4 type clinopyroxenes, can be identified as existing in equilibrium with their respective melts, while other clinopyroxenes may have crystallized from more evolved magma, with $Kd^{Fe-Mg} = 0.36-0.61$. The green core Kd^{Fe-Mg} values of B3 type clinopyroxenes can up to 1.08, and the rim Kd^{Fe-Mg} values of B3 type clinopyroxenes are more similar to the equilibrium condition of $Kd^{Fe-Mg} = 0.35-0.42$.

The average Kd^{Fe-Mg} value of A1 type clinopyroxenes in trachyandesite is 0.14, which suggests that these clinopyroxenes are better classified as antecrysts that originated from basaltic magma.

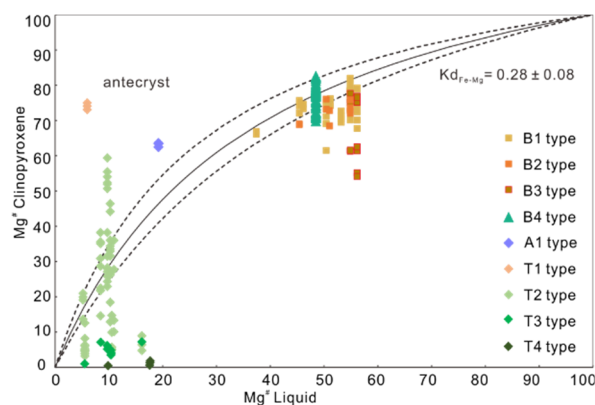


Figure 7. Equilibrium test diagram of clinopyroxene-melt. The bold and regular continuous lines define the equilibrium curves between clinopyroxene and the melt.

The Kd^{Fe-Mg} values of clinopyroxenes in the comenditic trachyte suggest that more than 2/3 of clinopyroxenes are in disequilibrium with the host melt. T1 type clinopyroxenes and some T2 type clinopyroxenes have lower Kd^{Fe-Mg} values and higher $Mg^\#$, these clinopyroxenes are plotted above the equilibrium curve corresponding to the whole-rock $Mg^\#$, where the $Mg^\#$ values of T1 type clinopyroxenes reach up to 75, showing obvious antecryst characteristics. The T2 type clinopyroxenes with high $Mg^\# = 51-60$ are usually trapped in alkali feldspar phenocrysts, which also reflects earlier crystallization compared to alkali feldspar phenocrysts. The other T2 type clinopyroxenes below the equilibrium curve are suggested to be derived from more evolved melts, with similar results found for T3 and T4 type clinopyroxenes (Figure 7).

Overall, the morphologically and compositionally diverse clinopyroxenes reveal the complexity of the volcanic plumbing system beneath the Sanshui Basin. The part B1, B4, and B2 type clinopyroxenes represent the autocrystic crystals from the equilibrium host magma; the green cores with low $Mg^\#$ value and rims with high $Mg^\#$ values in the B3 type clinopyroxenes reveal magma mixing, while the multi-phase zoning clinopyroxenes in the B4 type clinopyroxenes indicates the existence of magma recharge by other components [24]. The A1 type clinopyroxenes in trachyandesite and T1, and partial T2 type clinopyroxenes in comenditic trachyte are antecrysts representing magma recharge and mixing, derived from early magma. The B1, B2, T2, T3, and T4 type clinopyroxenes below the equilibrium curves of their host melts may represent crystal settling and convection from a more evolved magma during the continuous period of fractional crystallization.

6.2. Calculation of the Pressure-Temperature Conditions of Crystallization

One of the main objectives of volcanic petrological studies is reconstructing the depth of magma crystallization pre-eruption [41]. Many single clinopyroxene and clinopyroxene-equilibrium melt thermobarometers calibrated, pressures calculated by clinopyroxene-equilibrium melt may represent magma reservoir depths, which have been widely used in volcanic studies to constrain magma ascent and storage conditions. The temperature and pressure calculations for clinopyroxenes in basalt are in equilibrium with respective melts based on the Equations 30 and 33 [40], where the estimated average water content in basalt is 1.9% based on the Perinelli model [42]; disequilibrium was instead calculated according to Equations 32b and 32d [40]. In the comenditic trachyte, the temperature and pressure calculations of equilibrium clinopyroxenes are based on the Masotta model [43], with an initial water content of 4 wt.% [44]. The crystallization conditions of T3 and T4 type clinopyroxenes were not calculated because they represent crystals that are not in equilibrium. We speculate that these more evolved clinopyroxenes crystallize under a lower temperature and pressure conditions, based on alkaline feldspar-melt thermometric calculations [45].

The thermobarometric calculations are shown in Table S1 and Figure 8. The calculations show that clinopyroxene phenocrysts in the associated basalts of the Sanshui Basin feature lower crystallization depths and may have crystallized continuously during magma ascent through the crust. The deepest estimated depths of crystallization for basalt corresponds to the depths of the lithospheric mantle, while the crystallization depths of clinopyroxenes in comenditic trachyte corresponds to the depths of the upper crust.

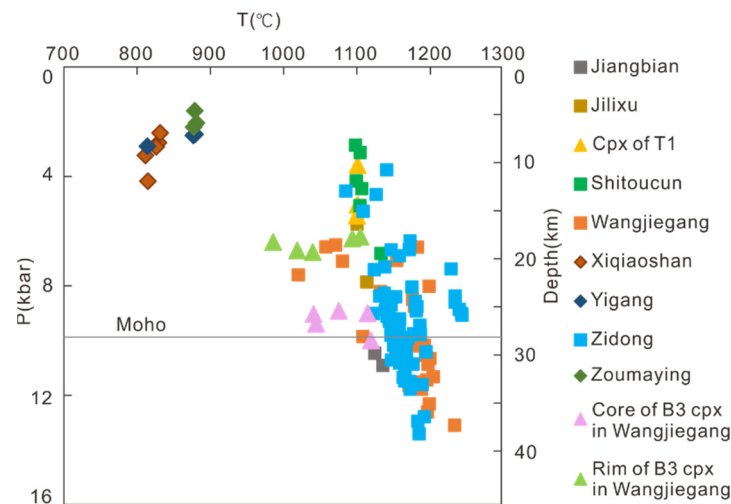


Figure 8. Temperatures and depths of crystallization of clinopyroxene phenocrysts in the bimodal volcanic rocks, calculated result using the clinopyroxene-liquid thermobarometer of Putirka [40] and Masotta [43]. Pressure to depth conversion is assumed to be 2.8 km/kbar [46].

6.3. Petrogenesis of Clinopyroxenes

6.3.1. Petrogenesis of B1 and B2 Type Clinopyroxenes

The B1 and B2 type clinopyroxenes are the most common types of basalt. Whilst the chemical composition varies widely in different sample locations, the overall composition remains relatively uniform, indicating crystallization in a relatively closed magma system. B1 and B2 type clinopyroxenes are characterized by lower $Mg^{\#}$ and Na_2O contents relative to clinopyroxenes from the Iherzolite xenolith (Figure 4), as well as a higher Ti/Al ratio and lower Al^{VI} value relative to clinopyroxenes from granulite xenolith, which is close to the composition of volcanic clinopyroxene in basalt (Figure 9).

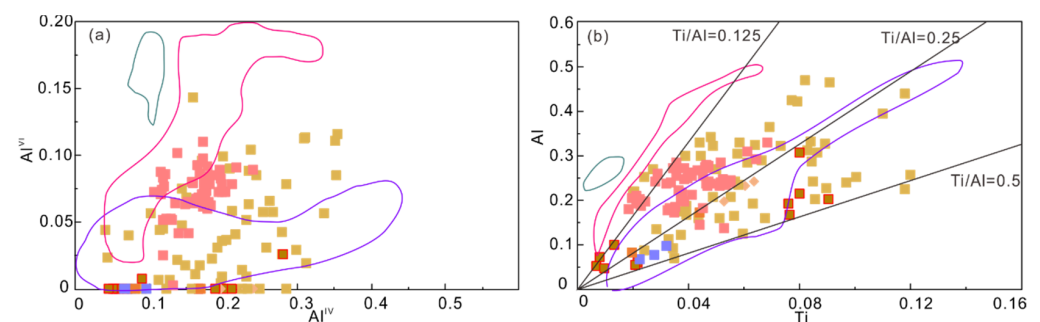


Figure 9. (a) Atomic proportion of Al^{VI} vs. Al^{IV} diagram in clinopyroxenes from basalt in the Sanshui Basin. (b) Atomic proportion of Ti vs. Al diagram. Symbols and data sources are the same as those of Figure 5.

We calculated the REE compositions of the parental magma for the B1 type clinopyroxene host basalt using the mineral-melt partition coefficients determined by Hart and Dunn [47]. According to the melt composition calculated by inversion, similar enrichment in LREE and no obvious Eu anomalies were observed relative to the whole rock composition. The whole rock composition of clinopyroxene was found to be well-matched with the

whole rock composition of 17ss066-1, 19ss023-1 (Figure 10a), indicating that clinopyroxenes were crystallized from the host magma, while some results (18ss082-1, 20ss025-1) were systematically horizontally distributed with the whole rock composition. A possible reason for this result may be that the partitioning coefficient varies with the changes in melt composition, temperature, pressure, redox conditions, or other factors [9]. The results for B2 type clinopyroxene are similar to those for B1 type clinopyroxene.

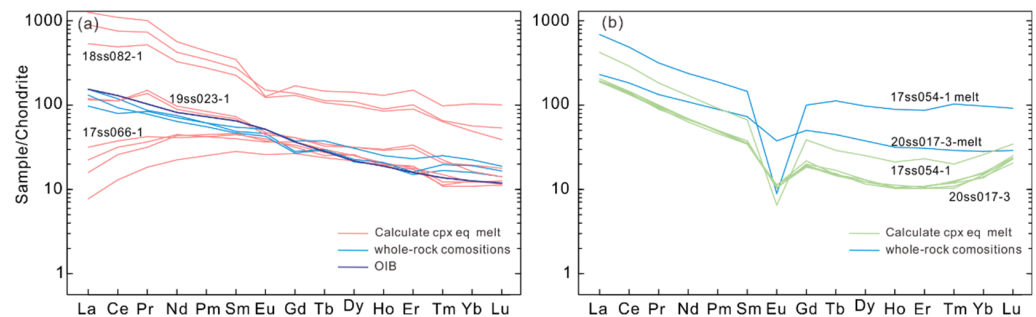


Figure 10. (a) Chondrite-normalized REE patterns for calculated melts of the basalt in the Sanshui Basin. (b) Chondrite-normalized REE patterns for calculated melts of the comenditic trachyte. The normalized values and OIB data are from [38]. The bulk rock data for the basalt and comenditic trachyte are from [28].

6.3.2. Petrogenesis of B3 Type Clinopyroxenes

The B3 type clinopyroxenes comprise a rare but compositionally distinct group of crystals that only in wangjiegang basalt samples. The composition shows reverse zoning, featuring a green core that is Fe-rich, Mg-poor, and has high REE contents with low Eu^*/Eu values, and a rim that is Mg-rich, Fe-poor, and has low REE contents, with low Eu^*/Eu values, indicating an open magma system. Green-core clinopyroxene, as indication of an open magma system, has been widely studied [13,14,48,49]. The genesis of green-core clinopyroxene mainly includes the following: (1) crystallization from a more evolved magma and subsequently mixing with mafic magma [8,14,49]; (2) xenoliths from the locally metasomatized upper mantle [50]; and (3) xenocrysts from the mantle, lower crust, or wall-rocks [13,51].

According to a comparison of major- and trace-element compositions of B3 type clinopyroxenes in basalts of the Sanshui Basin and clinopyroxenes in the lithospheric mantle peridotite in South China [34–36] and Hannuoba granulite in the North China Craton [35], green-core clinopyroxenes have different compositional characteristics similar to the B1 type clinopyroxenes. Therefore, the origin of green-core trapping from lithospheric mantle or lower crustal granulite can be excluded. Moreover, the resorption and sieved textures in the green core of B3 type clinopyroxene (Figure 2b) indicates that the genesis of green-core clinopyroxene is more strongly related to (1) the results of magma mixing and magma recharge. The $\text{Mg}^\#$ value in the core and rim of B3 type clinopyroxene is negatively correlated with Ti and Al content, and positively correlated with Eu anomalies. The REE distribution patterns of clinopyroxenes are also nearly parallel. Therefore, we propose that the green cores of B3 type clinopyroxenes crystallize from a more evolved melt at a shallow depth, while the rims of B3 type clinopyroxenes crystallizes from basaltic magma under near-equilibrium conditions.

6.3.3. Petrogenesis of B4 Type Clinopyroxenes

Based on the work of Zhang [24], Zidong basaltic magma begins to crystallize in alkaline basaltic magma, which is injected by tholeiitic magma to form zone 2, and then continues to crystallize in alkaline basaltic magma to form zone 1 and the rim, indicating earlier magma mixing and later fractional crystallization.

6.3.4. Petrogenesis of A1 and T1 Type Clinopyroxenes

A1 type clinopyroxenes in trachyandesite and T1 type clinopyroxenes in comenditic trachyte are antecrysts. Based on $Kd^{Fe-Mg} = 0.28$, the calculated equilibrium melt for A1 type clinopyroxene is $Mg^{\#} = 32$, which is higher than the value for the whole rock ($Mg^{\#} = 19$). Similarly, the equilibrium melt calculated for T1 type clinopyroxene is $Mg^{\#} = 45$, while the $Mg^{\#}$ of the whole-rock is only 6. In addition, the REE content of T1 type clinopyroxene and the lack of Eu anomalies are similar to the results for clinopyroxene in basalt (Figure 6, e.g.) indicating that these clinopyroxenes derived from basaltic magma.

6.3.5. Petrogenesis of T2 and T3 Type Clinopyroxenes

T2 type clinopyroxenes are the most abundant in comenditic trachyte, and the chemical compositions are also widely variable. As with the whole-rock compositions, T2 type clinopyroxenes exhibit significant negative Eu, Ti, and Sr anomalies in trace elements, which correlate with the unique partition coefficients of clinopyroxenes in alkaline melts [52]. Clinopyroxenes in alkaline magmatic systems are primitively calcic- in basaltic melts and trend toward sodic during fractional crystallization [38]. Due to the lack of Al^{IV} in T2 type clinopyroxenes, the addition of Na^+ atom creates charge balance with Fe^{3+} , as $Na^+ + Fe^{3+} \rightarrow 2Ca^{2+}$. The incorporation of REE^{3+} thus becomes more favorable with an increase in Fe^{3+} through the substitution of $REE^{3+} \rightarrow Fe^{3+}$. In addition, Olin [51] proposed that elevated D_{HREE} (Partition coefficient of HREE) in Fe-rich clinopyroxenes reflects enhanced compatibility relative to LREE, as the HREE have ionic radii more similar to Fe^{2+} and Mn^{2+} in sixfold coordination than Ca^{2+} in eightfold coordination, and HREE incorporating in both eightfold coordination (substituting for Na or Ca in M2 site) and sixfold coordination (substituting for Fe and Mn in M1 or M2 site). This result is consistent with the T2 type clinopyroxenes exhibiting a negative correlation between Fe, Mn vs. $Mg^{\#}$ (Figure 5) and the enrichment of HREE [52,53].

Based on the partition coefficients [32], the calculated REE compositions of the parental magma for the T2 type clinopyroxenes exhibit higher REE contents. Further, the REE pattern remains parallel up to the host rock, suggesting that T2 type clinopyroxene in 17ss054-1 and 20ss017-3 may have crystallized from evolved magma (Figure 10b).

The compositions of T3 type clinopyroxenes are similar to those of T2 type clinopyroxenes, with more obvious Eu anomalies, higher REE contents. All these chemical characteristics indicate that T3 type clinopyroxenes are results of the continuous evolution of T2 type clinopyroxenes.

6.3.6. Petrogenesis of T4 Type Clinopyroxenes

In contrast to other clinopyroxenes, the composition of T4 type clinopyroxenes trend toward an aegirine composition and may represent the endmember of clinopyroxene evolution (Figure 4b). However, lower LREE and total REE content was observed in T4 type clinopyroxenes compared to that in T3 type clinopyroxenes.

This result may be related to the unique incorporation mechanism of HREE and HFSE in the peralkaline system and the Na content in eightfold coordination (M2 site) with clinopyroxenes [54]. When M sites expand due to an increase in Aeg content, REE incorporation become less favorable, and when $Aeg > 50$ (mol%), although M sites shrink slightly, HREEs become strongly incorporated in sixfold coordination (M1 site), consistent with the increase in HREE concentration observed in aegirine ($Aeg > 80$, mol%) in T4 type clinopyroxenes.

Aegirine is a rare phase in peralkaline felsic volcanic rocks that occurs at temperatures below 700 °C [55,56], while the crystallization temperature of comenditic trachyte(14ss003-5) exceeds 850 °C. In addition, there is little research on the partition coefficients of aegirine. The REE contents and HFSE contents in aegirine from the Sanshui Basin are different from those aegirine in Romania [1] and Greenland [32], which feature higher REE contents and lower Zr-Hf contents, despite all these aegirines exhibit HREE enrichment relative to LREE

and positive Zr-Hf anomalies. The genesis of aegirine should be further elucidated through subsequent investigation.

6.4. Fractional Crystallization

As described above, the clinopyroxenes in basalt have similar geochemical compositions and REE patterns indicating that these clinopyroxenes crystallized from cogenetic magma. The clinopyroxenes in trachyandesite and T1, T2, and T3 type clinopyroxenes in comenditic trachyte have similar characteristics. Except for the obvious negative Eu anomalies, the A1, T1, T2, and T3 type clinopyroxenes in trachyandesite and comenditic trachyte have REE patterns parallel to those of clinopyroxenes in basalt, suggesting that clinopyroxenes in trachyandesite and comenditic trachyte crystallized from more evolved melts that evolved via basaltic magma. Combined with the linear trends of major elements of clinopyroxenes in bimodal volcanic rocks (Figure 5), we propose that all clinopyroxenes may crystallized from cogenetic magmas and that the compositional differences among the clinopyroxenes were, in turn, caused by different degrees of mineral fractional crystallization during magma evolution.

We applied the Rayleigh fractionation equation of $C_L = C_i \times (1 - F)^{(D-1)}$ to model the trace element behavior in clinopyroxenes during fractional crystallization, where C_L and C_i represent the trace element concentrations of the liquid and initial melt with clinopyroxenes; F is the fractionation degree of the parental melt; and D is the total partition coefficient based on the abundance and distribution coefficient of the fractional phase. Here, the equilibrium B1 type clinopyroxene in 17ss066-3 represents the primitive composition in basalt, with a higher $Mg^\#$ value and lower REE contents, while the equilibrium T2 type clinopyroxene in 20ss017-3. According to the mineral assemblage proportions of olive-clinopyroxene-plagioclase-apatite (20:10:68:2), we calculated the REE contents of clinopyroxene during fractional crystallization in basalt (Figure 11a). However, the calculated results show that the LREE and HREE contents do not match with T2 type clinopyroxene, possibly because the clinopyroxenes in basalt inherited the characteristics of different degrees of extraction from the mantle [34]. The mass balance calculation based on the above crystalline phase separation in the whole rock indicates a better relationship between 17ss066-3 and 20ss017-3 ($F = 0.75$, $r^2 = 0.53$) [45]. According to the alkaline feldspar-clinopyroxene-amphibole assemblage in a proportion of 80:10:10, REE elements match well except negative Eu anomaly (Figure 11a), indicating that T3 type clinopyroxenes are the results of the continuous evolution of T2 type clinopyroxenes in comenditic trachyte, followed by ~80% crystallization, which corresponds to the Mass balance calculation of the whole rock ($F = 0.88$, $r^2 = 0.73$) [45]. These results also explain why clinopyroxene phenocrysts have not been observed in the comendite and pantellerite with greater evolution, which may be related to the relatively heavy density of clinopyroxenes compared to the comenditic melt. During the comenditic and pantelleritic melt extraction processes, the clinopyroxenes settle through density differentiation at the bottom of comenditic trachyte magma chamber and finally erupts with comenditic trachyte [14]. Moreover, compared with the phenocryst content of 8–15% in comenditic trachyte, the phenocryst content in comendite and pantellerite with the greater evolution is characterized by poor crystal (<5%) in the petrography. In this study, we did not simulate the clinopyroxenes in trachyandesite, as these clinopyroxenes are in disequilibrium with the host rock.

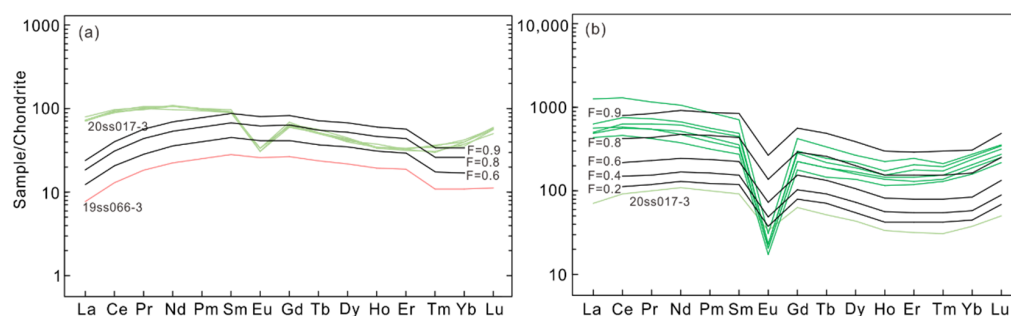


Figure 11. Inverse calculations of chondrite-normalized REE patterns of clinopyroxene produced by fractional crystallization. (a) based on the clinopyroxene from basalt compared with T2 type clinopyroxene from comenditic trachyte; (b) based on the T2 type clinopyroxene compared with T3 type clinopyroxene from comenditic trachyte. The evolution of these melts is modeled by variable proportion of fractional phases consist of olivine, clinopyroxene, plagioclase, apatite, alkaline feldspar, and arfvedsonite and the partition coefficients are listed in Table S3.

6.5. Magma Plumbing System

As described above, the texture and composition of clinopyroxene in bimodal volcanic rocks from the Sanshui Basin record the complex magmatic process pre-eruption. Moreover, the high abundance of B1 and B2 type clinopyroxenes in basalt and T2 type clinopyroxenes in comenditic trachyte record the fractional crystallization during magma evolution. The reversed zoning in B3 and B4 type clinopyroxenes records magma mixing and recharge in the basaltic magma chamber, while A1 type clinopyroxene and T1 type clinopyroxene record that more evolved melt mixed with basaltic melt, and T3 and T4 type clinopyroxenes record crystal settling and convection.

Notably, bimodal volcanic rocks in the Sanshui Basin are predominantly felsic end-member. Although the basalt has lower volume, it plays an important role in the magma evolution based on several factors: (1) The amount of basaltic magma, where the volume of parental melts required for high fractional crystallization is ~ 2.5 –5 times larger than the volume of felsic magma, especially for extreme fractional crystallization ($>90\%$) in the Sanshui Basin [57]; (2) the physical properties of basaltic magma, where the basalts feature lower viscosity and high density than felsic volcanic rocks. Consequently, the felsic magma reservoir is stored at a shallow depth on the roof of the magma reservoir, forming a barrier to prevent the basaltic magma from reaching the surface directly (Figure 12); (3) The supply rate of basaltic magma. A high supply rate of basaltic magma will make basalt as the dominant products. Conversely, a lower supply rate of basaltic magma may promote the evolution of peralkaline felsic magma [58]. This condition can be influenced and destroyed by the supply rate at any time, and an increased supply rate of basaltic magma can eventually trigger a volcanic eruption [59].

Based on thermobarometric calculations, we reconstructed the magma plumbing system of the Sanshui Basin (Figure 12). The proposed magma plumbing system consists of a homogeneous source mantle and various evolved magma reservoirs at different depths. In this system, asthenospheric mantle-derived magmas undergo fractional crystallization below the Moho to form basalts beneath the Sanshui Basin, and then ascend to shallow depths forming peralkaline felsic rocks via fractional crystallization or to the surface. Eventually, the peralkaline felsic rocks ascend to the surface and erupted.

Stage1: Mantle-derived magmas were produced, ascended and became stored in the lower crust and lithospheric mantle; these magmas then rapidly ascended to the surface and erupted with the phenocryst assemblage of olivine-clinopyroxene (B1, B2 type) -plagioclase. With a decrease of the liquidus, the clinopyroxenes became characterized by lower $Mg^{\#}$ values, higher REE contents, and the more obvious negative Eu anomalies during fractional crystallization.

Stage2: Magma recharge, characterized by the introduction of a primitive melt with high $Mg^{\#}$ and low REE content or mixing of a more primitive tholeiitic melt into an evolved

basaltic melt, formed reversed zoning textures of B3 and B4 type clinopyroxenes in an open system.

Stage3: Influenced by the supply rate of basaltic magma, basaltic magma evolved into felsic volcanic rocks at shallow depths via fractional crystallization after the early eruption. The source rock for felsic volcanism is related to basaltic magma and was formed by basaltic magma through continuous evolution and equilibrium crystallization of T2 type clinopyroxene. In this stage, T2 type clinopyroxenes crystallized from the comenditic trachytic melt, with lower Mg[#] values, higher REE contents, and the more obvious negative Eu anomalies.

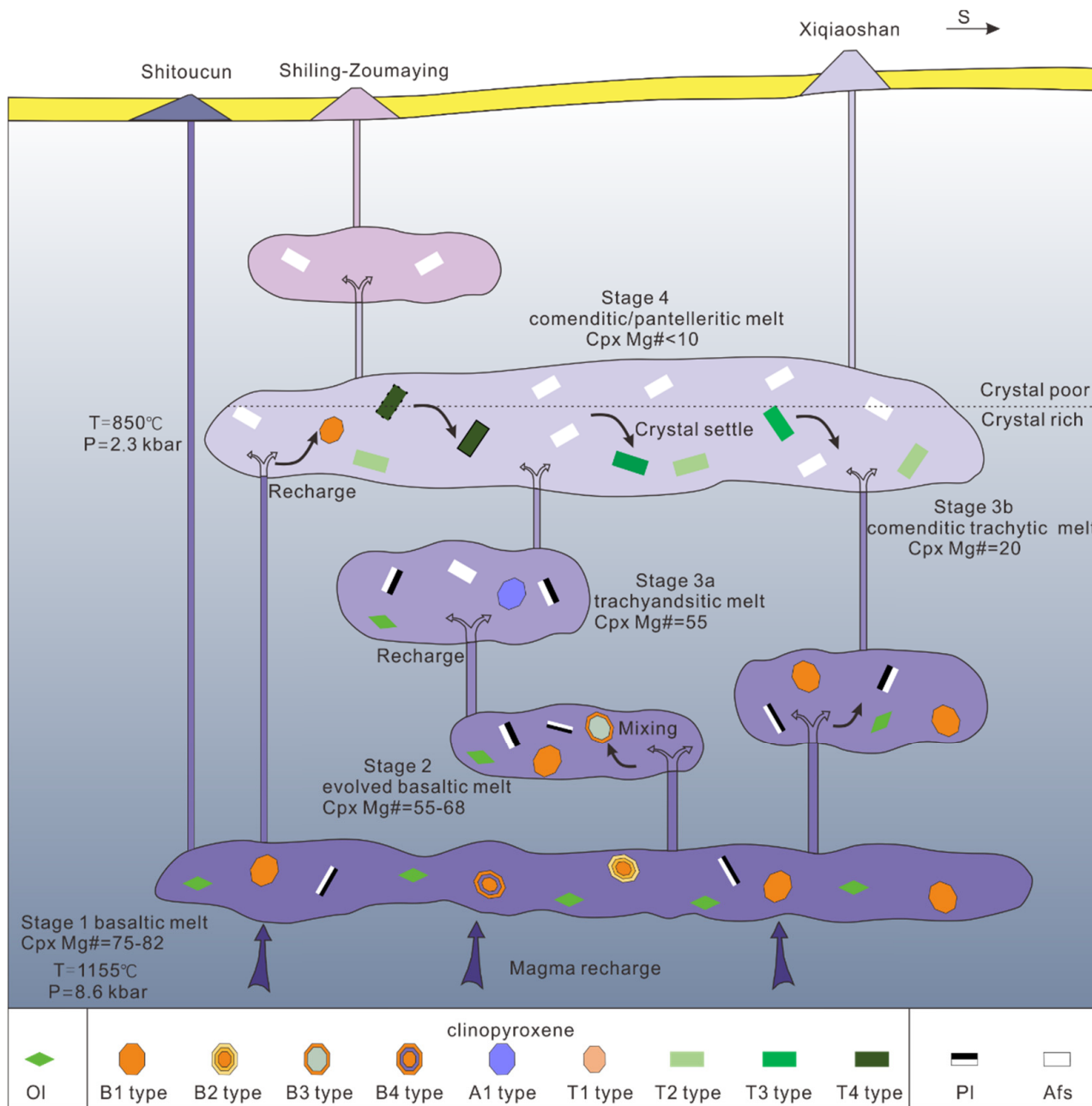


Figure 12. Schematic model of the magmatic processes of the alkaline magma system in the Sanshui Basin.

During the ascent of basaltic melt, existing primitive clinopyroxenes (A1 and T1 type clinopyroxenes) were carried into the trachyandesitic magma reservoir and comenditic trachytic reservoir, these primitive clinopyroxenes settled and formed the antecrysts.

Stage4: The evolved melt composition controlled the chemical composition of clinopyroxenes in the shallow magma chamber. T3 type clinopyroxenes and T4 type clinopyroxenes (aegirine) are characterized by high Fe and Na content, low $Mg^{\#}$ value, and high REE contents. However, due to crystal settling and convection, these clinopyroxenes settled to the bottom of comenditic trachytic magma reservoir and eventually erupted to the surface with comenditic trachyte.

7. Conclusions

The texture and composition of various clinopyroxenes in bimodal volcanic rocks from the Sanshui Basin reveal the complexity of the deep magmatic process and the evolutionary history of magma ascent. Different clinopyroxene phenocrysts show magma processes in an open or closed system, including fractional crystallization, magma mixing, recharge, and crystal settling. This study shows that detailed mineral-scale analysis is very important to reconstruct the complex volcano plumbing systems.

- (1) Clinopyroxenes in bimodal volcanic rocks from the Sanshui Basin can be classified into nine types according to their optical characteristics, major and trace element contents, with four types in basalts, one type in trachyandesite, and four types in comenditic trachyte.
- (2) With the evolutionary sequence of basalt-trachyandesite-comenditic trachyte-comendite/pantellerite, while the clinopyroxenes present an evolutionary sequence of diopside-hedenbergite-aegirine, characterized by decrease in the $Mg^{\#}$ value and Eu^*/Eu and increase in the REE content during magma evolution.
- (3) The dominate abundance of B1, B2, T2 type clinopyroxenes involves fractional crystallization in a closed system. The reversed zoning of B3 type green-core clinopyroxenes and the multiple zoning of B4 type clinopyroxenes were derived from the open system during magma evolution. The antecrysts consisting of A1 and T1 type clinopyroxenes provide the evidence for magma mixing and magma recharge beneath the Sanshui Basin.
- (4) Thermobarometric calculations in bimodal volcanic rocks from the Sanshui Basin show that clinopyroxene crystallized at several structural levels in the crust during magma ascent. Further, the basaltic magma reservoirs are distributed from lithospheric mantle (~40 km) to the upper crust (~10 km), and the comenditic trachyte reservoir is distributed in the upper crust (5–10 km).

Supplementary Materials: The following are available online at <https://www.mdpi.com/article/10.3390/min11111295/s1>. Table S1 Electron microprobe analyses of clinopyroxenes and thermobarometric calculations based on Putirka [40] and Masotta et al. [43] model for the bimodal volcanic rocks in the Sanshui Basin, Table S2 LA-ICP-MS analyses of clinopyroxenes for the bimodal volcanic rocks in the Sanshui Basin, Table S3 Values of partition coefficients (K_d) used in fractional crystallization modeling and the calculation of equilibrium melts.

Author Contributions: Conceptualization, P.C. and N.F.; methodology, P.C.; investigation, P.C. and X.Y.; resources, N.F.; writing-original draft preparation, P.C.; writing-review and editing, N.F. and X.Y.; visualization, N.F.; supervision, N.F.; project administration, N.F.; funding acquisition, N.F. All authors have read and agreed to the published version of the manuscript.

Funding: This research was funded by National Natural Science Foundation of China (No. 41572207).

Data Availability Statement: Some of the data presented in this study are available in the Supplementary Materials, Tables S1–S3.

Acknowledgments: We are grateful to Xianqiu Zhang, Wei Zhang, Yu Zhang, Yang Liu, and Heping Sun for their help in the field and pervious works. We thank Hui Zhang for help in EDS and BSE image at ECUT, Jinhua Hao for his help in EPMA at CUGB, Qian Wang for her help in LA-ICP-MS at CAGS.

Conflicts of Interest: The authors declare no conflict of interest.

References

1. Batki, A.; Pál-Molnár, E.; Jankovics, M.É.; Kerr, A.C.; Kiss, B.; Markl, G.; Heincz, A.; Harangi, S. Insights into the evolution of an alkaline magmatic system: An in situ trace element study of clinopyroxenes from the Ditrău Alkaline Massif, Romania. *Lithos* **2018**, *300*, 51–71. [[CrossRef](#)]
2. Coote, A.; Shane, P. Open-system magmatic behaviour beneath monogenetic volcanoes revealed by the geochemistry, texture and thermobarometry of clinopyroxene, Kaikohe-Bay of Islands volcanic field (New Zealand). *J. Volcanol. Geoth. Res.* **2018**, *368*, 51–62. [[CrossRef](#)]
3. Rossi, S.; Petrelli, M.; Morgavi, D.; Vetere, F.P.; Almeev, R.R.; Astbury, R.L.; Perugini, D. Role of magma mixing in the pre-eruptive dynamics of the Aeolian Islands volcanoes (Southern Tyrrhenian Sea, Italy). *Lithos* **2019**, *324*, 165–179. [[CrossRef](#)]
4. Perugini, D.; Poli, G. The mixing of magmas in plutonic and volcanic environments: Analogies and differences. *Lithos* **2012**, *153*, 261–277. [[CrossRef](#)]
5. Streck, M.J.; Dungan, M.A.; Malavassi, E.; Reagan, M.K.; Bussy, F. The role of basalt replenishment in the generation of basaltic andesites of the ongoing activity at Arenal volcano, Costa Rica: Evidence from clinopyroxene and spinel. *B. Volcanol.* **2002**, *64*, 316–327. [[CrossRef](#)]
6. Hughes, G.E.; Petrone, C.M.; Downes, H.; Varley, N.R.; Hammond, S.J. Mush remobilisation and mafic recharge: A study of the crystal cargo of the 2013–17 eruption at Volcán de Colima, Mexico. *J. Volcanol. Geoth. Res.* **2021**, *416*, 107296. [[CrossRef](#)]
7. Nakagawa, M.; Wada, K.; Wood, C. Mixed magmas, mush chambers and eruption triggers: Evidence from zoned clinopyroxene phenocrysts in andesitic scoria from the 1995 eruptions of Ruapehu volcano, New Zealand. *J. Petrol.* **2002**, *43*, 2279–2303. [[CrossRef](#)]
8. Streck, M.J. Mineral Textures and Zoning as Evidence for Open System Processes. *Rev. Mineral. Geochem.* **2008**, *69*, 595–622. [[CrossRef](#)]
9. Mollo, S.; Blundy, J.; Scarlato, P.; De Cristofaro, S.P.; Tecchiato, V.; Di Stefano, F.; Vetere, F.; Holtz, F.; Bachmann, O. An integrated P-T-H₂O-lattice strain model to quantify the role of clinopyroxene fractionation on REE plus Y and HFSE patterns of mafic alkaline magmas: Application to eruptions at Mt. Etna. *Earth-Sci. Rev.* **2018**, *185*, 32–56. [[CrossRef](#)]
10. Nazzareni, S.; Molin, G.; Peccerillo, A.; Zanazzi, P. Volcanological implications of crystal-chemical variations in clinopyroxenes from the Aeolian Arc, Southern Tyrrhenian Sea (Italy). *B. Volcanol.* **2001**, *63*, 73–82. [[CrossRef](#)]
11. Chen, L.; Zheng, Y.; Zhao, Z. Geochemical insights from clinopyroxene phenocrysts into the effect of magmatic processes on petrogenesis of intermediate volcanics. *Lithos* **2018**, *316*, 137–153. [[CrossRef](#)]
12. Di Stefano, F.; Mollo, S.; Ubide, T.; Petrone, C.M.; Caulfield, J.; Scarlato, P.; Nazzari, M.; Andronico, D.; Del Bello, E. Mush cannibalism and disruption recorded by clinopyroxene phenocrysts at Stromboli volcano: New insights from recent 2003–2017 activity. *Lithos* **2020**, *360*, 105440. [[CrossRef](#)]
13. Jankovics, M.E.; Taracsak, Z.; Dobosi, G.; Embey-Isztin, A.; Batki, A.; Harangi, S.; Hauenberger, C.A. Clinopyroxene with diverse origins in alkaline basalts from the western Pannonian Basin: Implications from trace element characteristics. *Lithos* **2016**, *262*, 120–134. [[CrossRef](#)]
14. Leite De Oliveira, A.; Costa Dos Santos, A.; Nogueira, C.C.; Maia, T.M.; Geraldés, M.C. Green core clinopyroxenes from Martin Vaz Archipelago Plio-Pleistocene alkaline rocks, South Atlantic Ocean, Brazil: A magma mixing and polybaric crystallization record. *J. S. Am. Earth Sci.* **2021**, *105*, 102951. [[CrossRef](#)]
15. Li, X.; Zeng, Z.; Yang, H.; Zhao, Y.; Yin, X.; Wang, X.; Chen, S.; Qi, H.; Guo, K. Integrated major and trace element study of clinopyroxene in basic, intermediate and acidic volcanic rocks from the middle Okinawa Trough: Insights into petrogenesis and the influence of subduction component. *Lithos* **2020**, *352*, 105320. [[CrossRef](#)]
16. Oung, T.N.; Ray, J.; Ghosh, B.; Koeberl, C.; Topa, D.; Paul, M. Clinopyroxene composition of volcanics from the Manipur Ophiolite, Northeastern India: Implications to geodynamic setting. *Int. J. Earth Sci.* **2018**, *107*, 1215–1229. [[CrossRef](#)]
17. Svetov, S.A.; Chazhengina, S.Y.; Stepanova, A.V. Geochemistry and Texture of Clinopyroxene Phenocrysts from Paleoproterozoic Picrobasalts, Karelian Craton, Fennoscandian Shield: Records of Magma Mixing Processes. *Minerals* **2020**, *10*, 434. [[CrossRef](#)]
18. Ubide, T.; Gale, C.; Arranz, E.; Lago, M.; Larrea, P. Clinopyroxene and amphibole crystal populations in a lamprophyre sill from the Catalan Coastal Ranges (NE Spain): A record of magma history and a window to mineral-melt partitioning. *Lithos* **2014**, *184*, 225–242. [[CrossRef](#)]
19. Villaseca, C.; García Serrano, J.; Orejana, D. Pyroxenites and Megacrysts From Alkaline Melts of the Calatrava Volcanic Field (Central Spain): Inferences From Trace Element Geochemistry and Sr-Nd Isotope Composition. *Front. Earth Sci.* **2020**, *8*, 132. [[CrossRef](#)]
20. Welsch, B.; Hammer, J.; Baronnet, A.; Jacob, S.; Hellebrand, E.; Sinton, J. Clinopyroxene in postshield Haleakala ankaramite: 2. Texture, compositional zoning and supersaturation in the magma. *Contrib. Mineral. Petr.* **2016**, *171*, 1–19. [[CrossRef](#)]
21. Zhu, B.; Wang, H.; Chen, Y.; Chang, X.; Hu, Y.; Xie, J. Geochronological and geochemical constraint on the Cenozoic extension of Cathaysian lithosphere and tectonic evolution of the border sea basins in East Asia. *J. Asian Earth Sci.* **2004**, *24*, 163–175.
22. Chung, S.; Cheng, H.; Jahn, B.; O'Reilly, S.Y.; Zhu, B. Major and trace element, and Sr-Nd isotope constraints on the origin of Paleogene volcanism in South China prior to the South China Sea opening. *Lithos* **1997**, *40*, 203–220. [[CrossRef](#)]
23. Zhou, H.; Xiao, L.; Dong, Y.; Wang, C.; Wang, F.; Ni, P. Geochemical and geochronological study of the Sanshui basin bimodal volcanic rock suite, China: Implications for basin dynamics in southeastern China. *J. Asian Earth Sci.* **2009**, *34*, 178–189. [[CrossRef](#)]

24. Zhang, W.; Fang, N.; Yuan, X.; Cui, L. Geochemical and Mineralogical Investigation on Different Types of Cenozoic Basalts in the Sanshui Basin: Implications for Magma Mixing Processes. *J. Earth Sci-China* **2019**, *30*, 754–762. [[CrossRef](#)]
25. Hou, M.; Ling, L.; Chen, H. *Sedimentary and Tectonic evolution of Sanshui Basin, Guangdong Province*; Geological Publishing House: Beijing, China, 2010; pp. 62–64. (in Chinese)
26. Zhang, X.; Zhou, X.; Chen, X. *Division and correlation Atlas of Cretaceous-Tertiary drilling strata in Sanshui Basin*; Ocean Press: Beijing, China, 1993; p. 179. (in Chinese)
27. Huang, H.; Guo, X.; Xia, S.; Qiu, X. Study of Crustal Thickness and Poisson's Ratio in the Coastal Area of South China. *Chin. J. Geophys.* **2014**, *57*, 860–871.
28. Yuan, X. The record of cenozoic magmatism in Sanshui Basin and its relationship with the early tectonic evolution stage of the South China Sea. Ph.D Thesis, China University of Geosciences (Beijing), Beijing, China, 2019.
29. Zhang, Y.; Fang, N. Source characteristics of basalts in Sanshui Basin and the early tectonic evolution stage of the South China Sea. *Mar. Geol. Quat. Geol.* **2021**, *41*, 95–113, (in Chinese with English abstract).
30. Liu, Y.; Hu, Z.; Gao, S.; Günther, D.; Xu, J.; Gao, C.; Chen, H. In situ analysis of major and trace elements of anhydrous minerals by LA-ICP-MS without applying an internal standard. *Chem. Geol.* **2008**, *257*, 34–43. [[CrossRef](#)]
31. Liu, Y.; Hu, Z.; Zong, K.; Gao, C.; Gao, S.; Xu, J.; Chen, H. Reappraisal and refinement of zircon U-Pb isotope and trace element analyses by LA-ICP-MS. *Chin. Sci. Bull.* **2010**, *55*, 1535–1546. [[CrossRef](#)]
32. Marks, M.; Halama, R.; Wenzel, T.; Markl, G. Trace element variations in clinopyroxene and amphibole from alkaline to peralkaline syenites and granites: Implications for mineral-melt trace-element partitioning. *Chem. Geol.* **2004**, *211*, 185–215. [[CrossRef](#)]
33. Morimoto, N.; Fabries, J.; Ferguson, A.K.; Ginzburg, I.V.; Ross, M.; Seifert, F.A.; Zussman, J.; Aoki, K.; Gottardi, G. Nomenclature of pyroxenes. *Am. Mineral.* **1988**, *73*, 1123–1133.
34. Zhang, H.; Zheng, J.; Pan, S.; Lu, J.; Li, Y.; Xiang, L.; Lin, A. Compositions and processes of lithospheric mantle beneath the west Cathaysia block, southeast China. *Lithos* **2017**, *286*, 241–251. [[CrossRef](#)]
35. Geng, X.; Liu, Y.; Zhang, W.; Wang, Z.; Hu, Z.; Zhou, L.; Liang, Z. The effect of host magma infiltration on the Pb isotopic systematics of lower crustal xenolith: An in-situ study from Hannuoba, North China. *Lithos* **2020**, *366–367*, 105556. [[CrossRef](#)]
36. Zhang, H.; Zheng, J.; Lu, J.; Pan, S.; Zhao, Y.; Lin, A.; Xiang, L. Composition and evolution of the lithospheric mantle beneath the interior of the South China Block: Insights from trace elements and water contents of peridotite xenoliths. *Contrib. Mineral. Petr.* **2018**, *173*, 53. [[CrossRef](#)]
37. Wang, X.; Li, Z.; Li, X.; Li, J.; Liu, Y.; Long, W.; Zhou, J.; Wang, F. Temperature, Pressure, and Composition of the Mantle Source Region of Late Cenozoic Basalts in Hainan Island, SE Asia: A Consequence of a Young Thermal Mantle Plume close to Subduction Zones? *J. Petrol.* **2012**, *53*, 177–233. [[CrossRef](#)]
38. Sun, S.S.; McDonough, W.F. Chemical and isotopic systematics of oceanic basalts: Implications for mantle composition and processes. *Geol. Soc. Lond. Spec. Publ.* **1989**, *42*, 313–345. [[CrossRef](#)]
39. Davidson, J.P.; Morgan, D.J.; Charlier, B.L.A.; Harlou, R.; Hora, J.M. Microsampling and Isotopic Analysis of Igneous Rocks: Implications for the Study of Magmatic Systems. *Annu. Rev. Earth. Pl. Sc.* **2007**, *35*, 273–311. [[CrossRef](#)]
40. Putirka, K.D. Thermometers and Barometers for Volcanic Systems. *Rev. Mineral. Geochem.* **2008**, *69*, 61–120. [[CrossRef](#)]
41. Kluegel, A.; Day, S.; Schmid, M.; Faria, B. Magma Plumbing During the 2014–2015 Eruption of Fogo (Cape Verde Islands). *Front. Earth Sci.* **2020**, *8*, 157. [[CrossRef](#)]
42. Perinelli, C.; Mollo, S.; Gaeta, M.; De Cristofaro, S.P.; Palladino, D.M.; Armienti, P.; Scarlato, P.; Putirka, K.D. An improved clinopyroxene-based hygrometer for Etnean magmas and implications for eruption triggering mechanisms. *Am. Mineral.* **2016**, *101*, 2774–2777. [[CrossRef](#)]
43. Masotta, M.; Mollo, S.; Freda, C.; Gaeta, M.; Moore, G. Clinopyroxene-liquid thermometers and barometers specific to alkaline differentiated magmas. *Contrib. Mineral. Petr.* **2013**, *166*, 1545–1561. [[CrossRef](#)]
44. Forni, F.; Degruyter, W.; Bachmann, O.; De Astis, G.; Mollo, S. Long-term magmatic evolution reveals the beginning of a new caldera cycle at Campi Flegrei. *Sci. Adv.* **2018**, *4*, eaat9401. [[CrossRef](#)]
45. Chen, P.; Fang, N.; Wang, Z.; Yuan, X. Petrogenesis and tectonic implications of Eocene peralkaline felsic volcanic rocks from the Sanshui Basin, Southern China. *Lithos* **2021**. under review.
46. Tao, Y.; Putirka, K.; Hu, R.; Li, C. The magma plumbing system of the Emeishan large igneous province and its role in basaltic magma differentiation in a continental setting. *Am. Mineral.* **2015**, *100*, 2509–2517. [[CrossRef](#)]
47. Hart, S.R.; Dunn, T. Experimental cpx/melt partitioning of 24 trace elements. *Contrib. Mineral. Petr.* **1993**, *113*, 1–8. [[CrossRef](#)]
48. Ziem À Bidias, L.A.; Chauhan, H.; Mekala, R.M.; Rao, N.V.C. Green core clinopyroxenes from basanites of Petpenoun volcanoes, Noun Plain, Cameroon volcanic line: Chemistry and genesis. *B. Volcanol.* **2021**, *83*, 13. [[CrossRef](#)]
49. Neumann, E.R.; Wulff-Pedersen, E.; Simonsen, S.L.; Pearson, N.J.; Martí, J.; Mitjavila, J. Evidence for Fractional Crystallization of Periodically Refilled Magma Chambers in Tenerife, Canary Islands. *J. Petrol.* **1999**, *40*, 1089–1123. [[CrossRef](#)]
50. Pilet, S.; Hernandez, J.; Villemant, B. Evidence for high silicic melt circulation and metasomatic events in the mantle beneath alkaline provinces: The Na-Fe-augitic green-core pyroxenes in the Tertiary alkali basalts of the Cantal massif (French Massif Central). *Miner. Petrol.* **2002**, *76*, 39–62. [[CrossRef](#)]
51. Zhu, Y.; Ogasawara, Y. Clinopyroxene phenocrysts (with green salite cores) in trachybasalts: Implications for two magma chambers under the Kokchetav UHP massif, North Kazakhstan. *J. Asian Earth Sci.* **2004**, *22*, 517–527. [[CrossRef](#)]

52. Baudouin, C.; France, L.; Boulanger, M.; Dalou, C.; Devidal, J. Trace element partitioning between clinopyroxene and alkaline magmas: Parametrization and role of M1 site on HREE enrichment in clinopyroxenes. *Contrib. Mineral. Petr.* **2020**, *175*, 42. [[CrossRef](#)]
53. Olin, P.H.; Wolff, J.A. Rare earth and high field strength element partitioning between iron-rich clinopyroxenes and felsic liquids. *Contrib. Mineral. Petr.* **2010**, *160*, 761–775. [[CrossRef](#)]
54. Bonechi, B.; Perinelli, C.; Gaeta, M. Clinopyroxene growth rates at high pressure: Constraints on magma recharge of the deep reservoir of the Campi Flegrei Volcanic District (south Italy). *B. Volcanol.* **2019**, *82*, 5. [[CrossRef](#)]
55. Macdonald, R.; Bagiński, B.; Leat, P.T.; White, J.C.; Dzierżanowski, P. Mineral stability in peralkaline silicic rocks: Information from trachytes of the Menengai volcano, Kenya. *Lithos* **2011**, *125*, 553–568. [[CrossRef](#)]
56. Di Carlo, I.; Rotolo, S.G.; Scaillet, B.; Buccheri, V.; Pichavant, M. Phase Equilibrium Constraints on Pre-eruptive Conditions of Recent Felsic Explosive Volcanism at Pantelleria Island, Italy. *J. Petrol.* **2010**, *51*, 2245–2276. [[CrossRef](#)]
57. Barker, S.J.; Wilson, C.J.N.; Baker, J.A.; Millet, M.A.; Rotella, M.D.; Wright, I.C.; Wysoczanski, R.J. Geochemistry and Petrogenesis of Silicic Magmas in the Intra-Oceanic Kermadec Arc. *J. Petrol.* **2013**, *54*, 351–391. [[CrossRef](#)]
58. Ayalew, D.; Pik, R.; Bellahsen, N.; France, L.; Yirgu, G. Differential Fractionation of Rhyolites During the Course of Crustal Extension, Western Afar (Ethiopian Rift). *Geochem. Geophys. Geosyst.* **2019**, *20*, 571–593. [[CrossRef](#)]
59. Jeffery, A.J.; Gertisser, R.; Self, S.; Pimentel, A.; O'Driscoll, B.; Pacheco, J.M. Petrogenesis of the Peralkaline Ignimbrites of Terceira, Azores. *J. Petrol.* **2017**, *58*, 2365–2401. [[CrossRef](#)]